




## FAULT DIAGNOSIS AND FAULT TOLERANT CONTROL OF ASYNCHRONOUS MOTOR SPEED SENSOR COMBINED WITH DIFFERENT SPEED ESTIMATORS

Qiubo LI 

School of Marine and Electrical Engineering, Jiangsu Maritime Institute, Nanjing 40000, China

\*Corresponding author, e-mail: [13914750290@163.com](mailto:13914750290@163.com)

### Abstract

Accurate speed and flux estimation are important conditions for achieving high-performance and low-cost control. Therefore, this study first constructs a mathematical model and space vector pulse width modulation control method for asynchronous motors. Then, a simple speed estimator, an extended Kalman filter speed estimator, and a full-order magnetic flux observer speed estimator are established in the speed estimation module. Finally, based on the Euler voting algorithm, a fault diagnosis and fault-tolerant control method for speed sensors is designed. The results showed that under low-speed conditions, the average mean square errors of the speed estimators of the simple, extended Kalman filter, and full-order magnetic flux observer were 0.7969, 0.9134, and 2.2526, respectively. The first two speed estimators had better performance, while under medium to high-speed conditions, the latter two speed estimators had a lower average mean square error and better performance. When various faults occurred, the research method could quickly determine the best performing speed estimator for feedback and effectively display the speed fluctuations caused by the faults. Finally, it smoothly switched to the speed sensorless mode and controlled the speed error within  $-5r/min-5r/min$ .

Keywords: Euler voting algorithm, asynchronous motor, speed sensor, fault diagnosis, fault-tolerant control

## 1. INTRODUCTION

Due to the improvement of performance and efficiency of AC speed control systems, their application fields and scope are constantly expanding. The high-performance Asynchronous Motor (AM) speed control system can not only meet the energy-saving needs and improve energy efficiency but also adapt to the process requirements of industrial production and enhance China's automation level [1-3]. According to statistical results, about 69% of China's electricity consumption is consumed by electric motors, most of which are used to drive AMs [4]. AM has a simple structure, high reliability, and easy maintenance, and can adapt to various complex environments. It is currently a widely used driving equipment in industrial sites [5]. However, with the increasing demand for performance and control accuracy of speed control systems in modern industrial applications, these requirements make it difficult for control systems to meet them solely by improving hardware equipment performance. Therefore, it is even more necessary to address these requirements from a control perspective [6]. In addition, system failures can also affect the safety and stability of its operation [7]. Given this, researching Fault Diagnosis (FD) and Fault-Tolerant Control (FTC)

for AM is crucial for modern production in the industrial sector. In response to the above issues, this study first establishes an AM mathematical model and its control method and then constructs a speed estimator based on different speed methods. Finally, based on the Euler's Vote (ESV) algorithm, FD and FTC methods for velocity sensors are designed. This study aims to improve the performance and efficiency of motor systems and reduce economic costs while ensuring performance. This has a positive promoting effect on industrial applications and socio-economic development. Its innovation mainly has the following two points. The first point is to propose three speed estimators in the speed estimation module of AM: Simple Speed Estimation (SSE), Extended Kalman Filter (EKF), and Full-Order Magnetic Flux Observer (FOMFO), to achieve accurate speed estimation across the entire speed range. The second point is to design an AM speed sensor FD and FTC method based on the ESV algorithm, aiming to achieve safe and stable operation of AM with small speed errors even after a fault occurs.

## 2. RELATED WORKS

The AM control method can effectively control and maintain the electrodes, thereby extending the

service life of the motor, reducing the maintenance and replacement costs of the motor, and improving the reliability and stability of the equipment. Numerous scholars have conducted in-depth discussions and analyses on this matter. Layate et al. developed a dynamic control method and combined it with a maximum power point tracking controller to improve the performance of three-phase induction motors powered by photovoltaic systems. This method has become an ideal structure for remote areas, and simulation experiments have shown its universality [8]. Teguia et al. aimed to design effective robust control laws for indirect magnetic field orientation control devices, proposing integral sliding film control and fuzzy membrane control to ensure the effectiveness of permanent magnet AM in the normal operating region. Based on the linear quadratic regulator, the optimal feedback gain was given, which confirmed the feasibility of this method [9]. Daoudi et al. proposed two improved strategies for direct torque control of AM. One strategy was based on sine pulse width modulation and proportional integral regulator, while the other was based on sliding membrane control. Both methods could improve control performance and enhance the reliability of the entire system [10].

Due to various reasons, the control system may encounter various faults during operation, which poses a huge challenge to the stability and reliability of the system. FD and FTC technologies have emerged to address this issue. Li et al. achieved a composite diagnosis of traction motors based on a Support Vector Machine (SVM) combined with sensor technology to guarantee the safe operation of trains. This method improved the practical efficiency of FD [11]. Xia et al. proposed a nonlinear autoregressive model and limit learning machine to achieve a real-time FD method for unidirectional PWM rectifiers. Tests have shown that this method has fast fault detection speed and robustness to load fluctuations [12]. Gholipour et al. designed a current sensor FTC method without speed measurement to improve the reliability of induction motors. This method could improve the system's reliability and security in the event of a malfunction [13]. Shabbir et al. proposed a sensor FD and active FTC method based on an adaptive Radial Basis Function network for uncertain nonlinear systems. The feasibility and superiority of the research method have been verified [14].

In summary, current research achievements focus on vector control technology for AM and speed estimation using a single speed sensor, but a single method makes it difficult to achieve accurate estimation in various speed ranges. Therefore, this study designs an AM speed sensor FD and FTC method based on the ESV algorithm to solve the above problems.

mutual inductance between the stator and rotor. The voltage equation is shown in equation (3).

### 3. SPEED SENSORS FD AND FTC BASED ON ESV ALGORITHM

This study first constructs the control method and mathematical model of AM, then establishes speed estimators using different methods, and finally proposes speed sensor FD and FTC methods based on the ESV algorithm.

#### 3.1. Establishment of AM control method and mathematical model

AM is an AC motor that converts electromechanical energy into mechanical energy by generating electromagnetic torque through the interaction between the rotating magnetic field in the air gap and the induced current in the rotor winding. It accounts for about 90% of electric-powered machinery in various countries [15-16]. As a high-order, nonlinear, and strongly coupled multivariable system, it is difficult to control [17]. Therefore, this study uses vector control theory to convert vectors in a Three-Phase Coordinate System (TPCS) into DC variables in a two-phase rotating coordinate system, to control the Torque Current and Excitation Current (TC-EC) components corresponding to the stator current. Firstly, the AM model is constructed under TPCS, assuming that spatial harmonics, magnetic saturation, and iron losses need to be ignored. Normally, the AM model includes the equations of voltage, magnetic flux, electromagnetic torque, and electromechanical motion. The specific expressions for each equation are as follows. The calculation of the magnetic flux equation is shown in equation (1).

$$\begin{bmatrix} \alpha_A \\ \alpha_B \\ \alpha_C \\ \alpha_a \\ \alpha_b \\ \alpha_c \end{bmatrix} = \begin{bmatrix} i_A \\ i_B \\ i_C \\ i_a \\ i_b \\ i_c \end{bmatrix} \begin{bmatrix} Z_{AA} & Z_{AB} & Z_{AC} & Z_{Aa} & Z_{Ab} & Z_{Ac} \\ Z_{BA} & Z_{BB} & Z_{BC} & Z_{Ba} & Z_{Bb} & Z_{Bc} \\ Z_{CA} & Z_{CB} & Z_{CC} & Z_{Ca} & Z_{Cb} & Z_{Cc} \\ Z_{aA} & Z_{aB} & Z_{aC} & Z_{aa} & Z_{ab} & Z_{ac} \\ Z_{bA} & Z_{bB} & Z_{bC} & Z_{ba} & Z_{bb} & Z_{bc} \\ Z_{cA} & Z_{cB} & Z_{cC} & Z_{ca} & Z_{cb} & Z_{cc} \end{bmatrix} \quad (1)$$

In equation (1),  $\alpha_A$ ,  $\alpha_B$ ,  $\alpha_C$  and  $\alpha_a$ ,  $\alpha_b$ ,  $\alpha_c$  are the three-phase magnetic fluxes corresponding to the Stator Winding and Rotor Winding (SW&RW).  $Z_{AA}$ ,  $Z_{BB}$ ,  $Z_{CC}$ ,  $Z_{aa}$ ,  $Z_{bb}$ , and  $Z_{cc}$  are the self-inductance of the 3-phase windings corresponding to the stator and rotor.  $i_A$ ,  $i_B$ ,  $i_C$ ,  $i_a$ ,  $i_b$ , and  $i_c$  are the three-phase currents corresponding to the SW&RW. The letters below  $Z$  represent the mutual inductance of different windings. The torque equation is shown in equation (2)

$$F_e = n_1 Z_{dh} \{ \{ i_A i_a + i_B i_b + i_C i_c \} \sin \theta + \sin(\theta + 120^\circ) [ i_A i_b + i_B i_c + i_C i_a + i_A i_c + i_B i_a + i_C i_b ] \} \quad (2)$$

In equation (2),  $n_1$ ,  $\theta$ , and  $Z_{dh}$  correspond to the number of motor poles, angular displacement, and

$$\begin{bmatrix} U_A \\ U_B \\ U_C \\ U_a \\ U_b \\ U_c \end{bmatrix} = W \begin{bmatrix} \alpha_A \\ \alpha_B \\ \alpha_C \\ \alpha_a \\ \alpha_b \\ \alpha_c \end{bmatrix} + \begin{bmatrix} i_A \\ i_B \\ i_C \\ i_a \\ i_b \\ i_c \end{bmatrix} \begin{bmatrix} R_d & 0 & 0 & 0 & 0 & 0 \\ 0 & R_d & 0 & 0 & 0 & 0 \\ 0 & 0 & R_d & 0 & 0 & 0 \\ 0 & 0 & 0 & R_z & 0 & 0 \\ 0 & 0 & 0 & 0 & R_z & 0 \\ 0 & 0 & 0 & 0 & 0 & R_z \end{bmatrix} \quad (3)$$

In equation (3),  $U_A$ ,  $U_B$ ,  $U_C$  and  $U_a$ ,  $U_b$ ,  $U_c$  are the 3-phase voltages corresponding to the SW&RW.  $W$  is a differential operator.  $R_d$  and  $R_z$  are the resistances corresponding to the SW&RW. The equation of motion is shown in equation (4).

$$F_e = F_z + \frac{g}{n_1} W \omega \quad (4)$$

In equation (4),  $F_z$ ,  $g$ , and  $\omega$  correspond to load torque, moment of inertia, and rotor rotational angular velocity. The frequency conversion control method cannot have good dynamic performance. The above model indicates that it is a multivariate, strongly coupled mathematical equation, and therefore requires coordinate transformation processing for direct control in the future. The transformation of TPCS to a Two-phase Rotating Coordinate System (2RCS) involves two types: one is the transformation between a 3PCS and a 2-phase Stationary Coordinate System (2SCS), and the other is the transformation between a 2SCS and a 2RCS. The transformed AM mathematical model is as follows, and the expression of the magnetic flux equation is shown in equation (5).

$$\begin{bmatrix} \alpha_{d\chi} \\ \alpha_{d\delta} \\ \alpha_{z\chi} \\ \alpha_{z\delta} \end{bmatrix} = \begin{bmatrix} i_{d\chi} \\ i_{d\delta} \\ i_{z\chi} \\ i_{z\delta} \end{bmatrix} \begin{bmatrix} Z_d & 0 & Z_{dh} & 0 \\ 0 & Z_d & 0 & Z_{dh} \\ Z_{dh} & 0 & Z_z & 0 \\ 0 & Z_{dh} & 0 & Z_z \end{bmatrix} \quad (5)$$

In equation (5),  $\alpha_{d\chi}$ ,  $\alpha_{z\chi}$  and  $i_{d\chi}$ ,  $i_{z\chi}$  represent the magnetic flux and current between the stator and rotor on the  $\chi$ -axis.  $\alpha_{d\delta}$ ,  $\alpha_{z\delta}$  and  $i_{d\delta}$ ,  $i_{z\delta}$  are the currents of the stator and rotor under the  $\delta$ -axis.  $Z_d$  and  $Z_z$  are the inductance corresponding to the stator and rotor. The calculation of electromagnetic torque is shown in equation (6).

$$F_e = \frac{n_1 Z_{dh}}{Z_z} (i_{d\delta} \alpha_{z\chi} - i_{d\delta} \alpha_{z\delta}) \quad (6)$$

The expression for voltage is shown in equation (7).

$$\begin{bmatrix} u_{s\chi} \\ u_{s\delta} \\ 0 \\ 0 \end{bmatrix} = \begin{bmatrix} i_{s\chi} \\ i_{s\delta} \\ i_{z\chi} \\ i_{z\delta} \end{bmatrix} \begin{bmatrix} R_s + WZ_{dh} & -\omega_{xz}Z_{dh} & WZ_{dh} & -\omega_{xz}Z_{dh} \\ \omega_{xz}Z_d & R_s + WZ_{dh} & \omega_{xz}Z_{dh} & WZ_{dh} \\ WZ_{dh} & -(\omega_{xz} - \omega)Z_{dh} & R_r + WZ_z & -(\omega_{xz} - \omega)Z_z \\ (\omega_{xz} - \omega)Z_{dh} & WZ_{dh} & (\omega_{xz} - \omega)Z_z & R_r + WZ_z \end{bmatrix} \quad (7)$$

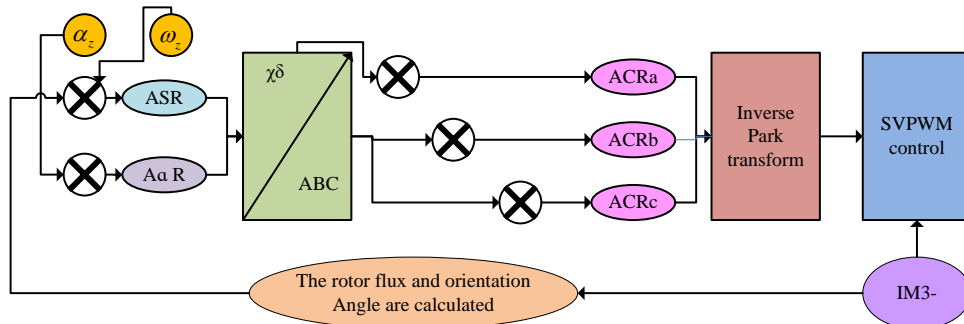


Fig. 1. AM closed-loop vector control system framework

In equation (7),  $u_{s\chi} / i_{s\chi}$  and  $u_{s\delta} / i_{s\delta}$  are the voltage and current of the stator on the  $\chi$ -axis and  $\delta$ .  $i_{z\chi}$  and  $i_{z\delta}$  are the rotor currents of the  $\chi$  and  $\delta$  axes.  $\omega_{xz}$  is the synchronous angular velocity of the stator rotating magnetic field.  $R_s$  and  $R_z$  are the stator resistance and rotor resistance. The vector control system measures and controls the AM stator current vector, and based on the principle of magnetic field orientation, controls the TC-EC separately to achieve the goal of controlling the AM torque. At this point, it is necessary to convert the coordinate system and define the axes where the torques in the same direction as the  $\chi$  and  $\delta$  axes in the original coordinate system are located as the  $E$  and  $T$  axes. From this, the corresponding expressions for speed and magnetic flux can be obtained, as shown in equation (8).

$$\begin{cases} W\alpha_{re} = -\frac{1}{T_c} \alpha_{re} + \alpha_{rt}(\omega_{xz} - \omega) + \frac{Z_{dh}}{T_c} i_{de} \\ W\alpha_{rt} = -\frac{1}{T_c} \alpha_{rt} + \alpha_{re}(\omega_{xz} - \omega) + \frac{Z_{dh}}{T_c} i_{dt} \end{cases} \quad (8)$$

In equation (8),  $T_c$ ,  $i_{de}$ , and  $i_{dt}$  are the time constants of the rotor and the stator currents corresponding to the  $E$ -axis and  $T$ -axis. The formula for electromagnetic torque is shown in equation (9).

$$F_e = \frac{n_1 Z_{dh}}{Z_z} i_{dt} \alpha_z \quad (9)$$

Based on the above content, the decoupling operation of AM stator current torque component and excitation component can be achieved, and the control of AM can be completed. The schematic diagram of the AM closed-loop vector control system framework is shown in Fig.1.

Among them, Space Vector Pulse Width Modulation (SVPWM) primarily utilizes the ideal magnetic flux circle of the stator of a 3-phase symmetrical motor supplied with a 3-phase symmetrical sine wave voltage as a reference standard. This is achieved by appropriately switching between various switching modes of the 3-phase inverter to form Pulse Width Modulation (PWM) [18-20]. In addition, SVPWM considers the inverter system and AM as a whole, making the model simpler and easier for real-time control by microprocessors. The simplified switch model and switch example of PWM inverter are shown in Fig.2.

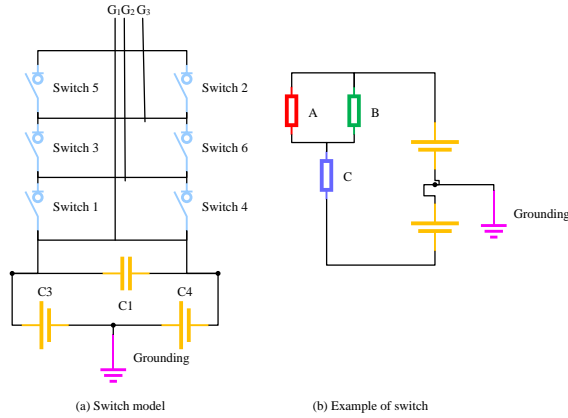


Fig. 2. Simplified switch model and switch example diagram of PWM inverter

In Figure 2,  $G_1 \sim G_3$  is the open state of three bridge arms, with the open states of the upper and lower bridge arms set to 1 and 0, respectively, for a total of 8 states.  $U_M$  is the bus voltage. Different states correspond to zero vector voltage, while other states generate voltage vectors of  $\frac{2U_M}{3}$ . In the switch example,  $G_1 = G_2 = 1$  and  $G_3 = 0$  are the equivalent circuit in the current switch state. Under various switch states, the inverter will generate corresponding voltage vectors. In addition, SVPWM arranges the pulse width time duty cycle in a sinusoidal pattern, so that the output waveform can achieve sinusoidal output after appropriate filtering. The specific schematic diagram is shown in Fig.3.

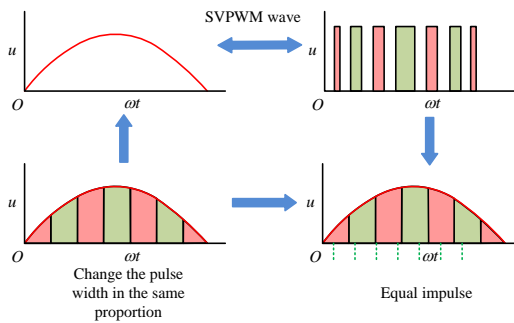


Fig. 3. Sine wave output process based on SVPWM technology

In Fig. 3, the sine half wave has  $N$  equal parts and is viewed as consisting of  $N$  interconnected pulses with equal widths but varying amplitudes in accordance with the sine curve. By replacing the

pulse area enclosed by each equal sine curve and the horizontal axis with a rectangular pulse of equal area, a corresponding rectangular pulse sequence can be obtained, which is equivalent to a sine half wave.

### 3.2. Speed estimation and FD and FTC based on ESV algorithm

The speed of the motor is an important parameter in the control system. In motor speed control, the speed estimator can effectively suppress various internal disturbances and improve the overall system's dynamics and robustness. However, various speed control methods currently cannot achieve precise control of the entire process. Therefore, research is being conducted on combining different speed estimation methods for control, and the ESV algorithm is used in each stage to select the more accurate method for speed control. Due to the advantages of simple implementation and high computational efficiency of SSE (F1), EKF (F2) can handle non-linear problems such as AM well and handle sensor noise, while FOMFO (F3) can perform speed estimation over a wide operating range. Therefore, this study chooses the above method for speed estimation. In F1, there is a difference of one slip speed between the AM speed and the synchronous speed, which results in the AM speed  $\omega_b$ , as shown in equation (10).

$$\omega_b = \omega_{br} - \omega_{\Delta} \quad (10)$$

In equation (10),  $\omega_{br}$  and  $\omega_{\Delta}$  are the AM synchronous speed and its slip speed. The expression for  $\omega_{\Delta}$  is shown in equation (11).

$$\omega_{\Delta} = \frac{Z_{dh}R_z \alpha_z \chi^i d\delta + \alpha_z \delta^i d\chi}{Z_z \alpha_z^2 \chi + \alpha_z^2 \delta} \quad (11)$$

The structure of the F1 speed estimator is shown in Fig.4.

F2 has two parts: the prediction stage and the correction stage. It mainly calculates the posterior probability distribution using Bayesian probability theory through the dynamic equations and observation equations of the system, linearizing the nonlinear system. The correction part requires calculating Kalman gain and updating the state and error covariance. Before the implementation of F2, it is necessary to discretize the AM model, as shown in equation (12).

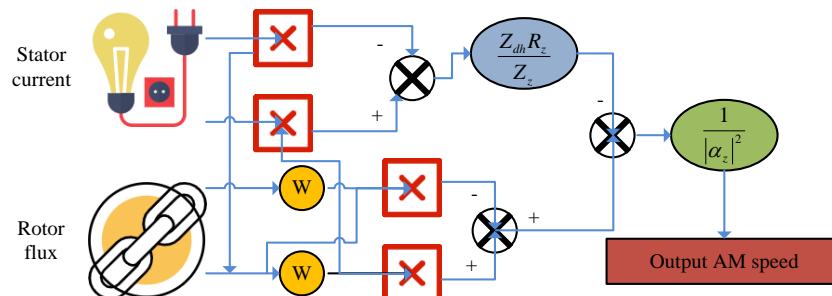


Fig. 4. Structure diagram of F1 speed estimator

$$\begin{cases} X_2(l) = D_1 X_2(l-1) + K_1 U_2(l-1) \\ Y_2(l) = C_1 X_2(l) \end{cases} \quad (12)$$

In equation (12),  $X_2(l)$  is the current state variable.  $U_2(l-1)$  is the input quantity from the previous moment.  $Y_2(l)$  and  $D_1$  are the output matrix and system matrix.  $K_1$  and  $C_1$  are both input matrices. After the above processing is completed, it can be run according to the Kalman filter process. The principle of F3 is as follows: if the input and output of the controlled object can be observed, the state can be reconstructed through a full-order state observer based on this, and the state variables to be calculated can be estimated. The rotor flux and stator current are state variables that need to be observed, and an AM model in a stationary coordinate system needs to be constructed, as shown in equation (13).

$$\begin{cases} WX_1 = D_1 X_1 + K_1 U_1 \\ Y_1 = C_1 X_1 \end{cases} \quad (13)$$

The FOMFO mathematical model of AM is shown in equation (14).

$$W\hat{X}_1 = \hat{D}_1 \hat{X}_1 + \hat{K}_1 \hat{U}_1 + Q(Y - C_1 \hat{X}) \quad (14)$$

In equation (14),  $Q$  is the gain matrix. In general, the poles of the observer and the AM poles exhibit a positive correlation, with a ratio greater than 1, to ensure the stability of establishing the observer. Fig.5 shows the F3 framework.

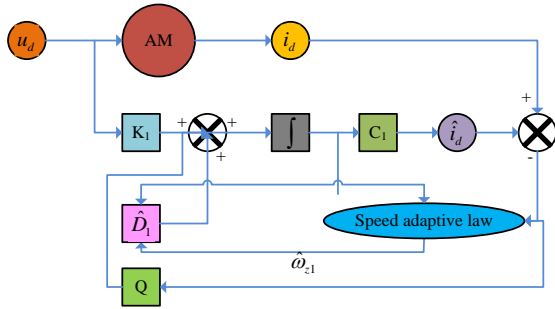


Fig. 5. Schematic diagram of F3 speed estimator principle

To further ensure the stability of the control system, this study designs an adaptive rate based on the Lyapunov stability theory. Firstly, the derivative of the Lyapunov function  $V$  is calculated using equation (15).

$$W = e^T W e + e W e^T + 2 \frac{(\omega_z - \hat{\omega}_{z1})}{\psi} W \hat{\omega}_{z1} \quad (15)$$

In equation (15),  $\psi$  is a constant and  $\hat{\omega}_{z1}$  is the estimated speed value. By subtracting the Lyapunov function from equation (15), the differential equation of observer error can be obtained. Under the influence of the gain matrix and the actual motor, the change in magnetic flux is zero, and then the estimated speed can be obtained. Finally, the proportional integral structure replaces the speed estimation value to obtain the adaptive law of the speed, as shown in equation (16).

$$\hat{\omega}_{z1} = \left( \frac{k_i}{s} + k_p \right) [\hat{\alpha}_{z\chi}(i_{a\delta} - i_{a\delta}) - \hat{\alpha}_{z\delta}(i_{a\chi} - i_{a\chi})] \quad (16)$$

In equation (16),  $S$ ,  $k_i$ , and  $k_p$  are complex variables, proportional coefficients, and integral coefficients. The proportional integral structure is

sensitive to parameter variations and uncertainties in modeling and measurement. Given this, Lyapunov theory is used for asymptotic stability processing, and the speed estimation value is obtained through the adaptive feedback of the error between the estimated value and the actual value and the rotor magnetic flux composition. In summary, the construction of speed estimators for different methods can be completed. After the completion of the speed estimation module design, when it malfunctions, appropriate methods need to be used for efficient and rapid diagnosis. Therefore, this study proposes FD and FTC methods based on ESV algorithm. The FD method and ESV algorithm of the AM speed sensor are shown in Fig.6.

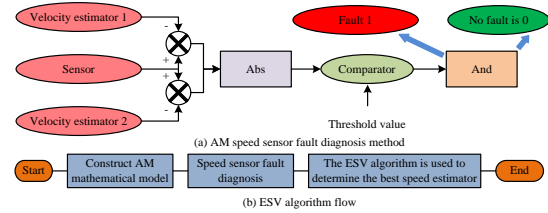


Fig. 6. AM speed sensor fault diagnosis method and ESV algorithm

In Fig.6, the three speed estimators compare the output sensor with the set threshold to determine if there is a fault. Output bit 1 indicates the presence of a fault, while the opposite is 0. In the ESV algorithm process, it is necessary to construct an AM speed sensor model, and then collect voltage, current, and speed signals. Finally, the algorithm can select the estimator with the smallest absolute error value as the feedback for the speed. In the FD section, the diagnostic strategy formula is shown in equation (17).

$$\begin{cases} |e_{F1}| = |\omega'_z - \hat{\omega}_{F1}| \\ |e_{F2}| = |\omega'_z - \hat{\omega}_{F2}| \\ |e_{F3}| = |\omega'_z - \hat{\omega}_{F3}| \end{cases} \quad (17)$$

In equation (17),  $|e_{F1}|$ ,  $|e_{F2}|$ , and  $|e_{F3}|$  are the absolute values of the errors of F1, F2, and F3. The estimated values corresponding to F1, F2, and F3 of  $\hat{\omega}_{F1}$ ,  $\hat{\omega}_{F2}$ , and  $\hat{\omega}_{F3}$ .  $\omega'_z$  is the measured value of the speed sensor. If the estimated values exceed the threshold, it indicates a fault and the output is 1, otherwise the output is 0. When a disconnection fault occurs at time  $t_0$ , the previous output value is normal, and the subsequent output values are all 0. When a fixed deviation fault occurs at time  $t_0$ , the output value will differ from the normal value by a constant thereafter. In the FTC section, when the above two types of faults occur, it is necessary to determine the speed feedback of different speed estimation methods through the ESV algorithm. The specific ESV algorithm calculation process is as follows: calculate the predicted value based on Euler approximation, compare it with the input value, and select the best speed estimation method, as shown in equation (18).

$$\omega_p(l) = 2\omega_z(l-1) - \omega_z(l-2) \quad (18)$$

In equation (18),  $\omega_z(l-1)$  and  $\omega_z(l-2)$  are the output values corresponding to the two time points on the AM speed sensor. When the AM speed sensor malfunctions, it needs to be divided into three stages: low speed, medium speed, and high speed. At each stage, it is essential to compare the predicted values with the estimated values of the two most accurate speed estimators for that stage. The speed estimator with the smallest absolute error should then be used as feedback on the speed, in order to facilitate FTC for faults in different speed stages.

#### 4. ANALYSIS OF FD AND FTC RESULTS BASED ON ESV ALGORITHM

To verify the effectiveness and feasibility of the research method, the performance of speed estimation modules based on different methods was compared to determine the best speed estimation method for different speed stages. Further simulations were conducted on the FD and FTC methods based on the ESV algorithm.

##### 4.1. Performance comparison of speed estimation modules based on different methods

To test the performance of individual different speed estimation methods, a 10kW AM speed sensor control platform is constructed for FD and FTC. The control core uses a high-performance floating-point digital signal processor TMS320VC33PGE150. The speed sensor uses a rotary encoder and is simulated using software Simulink. The simulation parameters are set as follows: the rated voltage, rated speed, and rated power of the AM are set to 380V, 1440r/min, and 4kW, respectively. The stator resistance and stator self inductance are set to 1.410 $\Omega$  and 0.182H. The rotor resistance and rotor self inductance are set to 1.139 $\Omega$  and 0.174H. The number of pole pairs is 2. The parameter settings for the speed estimator are as follows: the load torque is set to 10N\*m and rotor magnetic flux is set to 0.5Wb. The settings for different speed stages: low speed, medium speed, and high speed correspond to 120r/min, 500r/min, and 1200r/min, and the evaluation index is selected as Mean Square Error (MSE). Fig.7 shows the speed estimation and estimation error results based on different methods under different speed conditions.

Figures 7 (a) to (f) show a comparison of speed estimation using different methods at low, medium, and high speeds. 7 (a) and 7 (d) show that under low-speed conditions, the speed estimators corresponding to F1 and F2 have a higher degree of fit with the actual values. 7 (b) and 7 (e), 7 (c) and 7 (f) indicate that the speed estimators corresponding to F2 and F3 perform better under medium and high speed conditions. From this, it can be determined that F1 and F3 are selected under low-speed

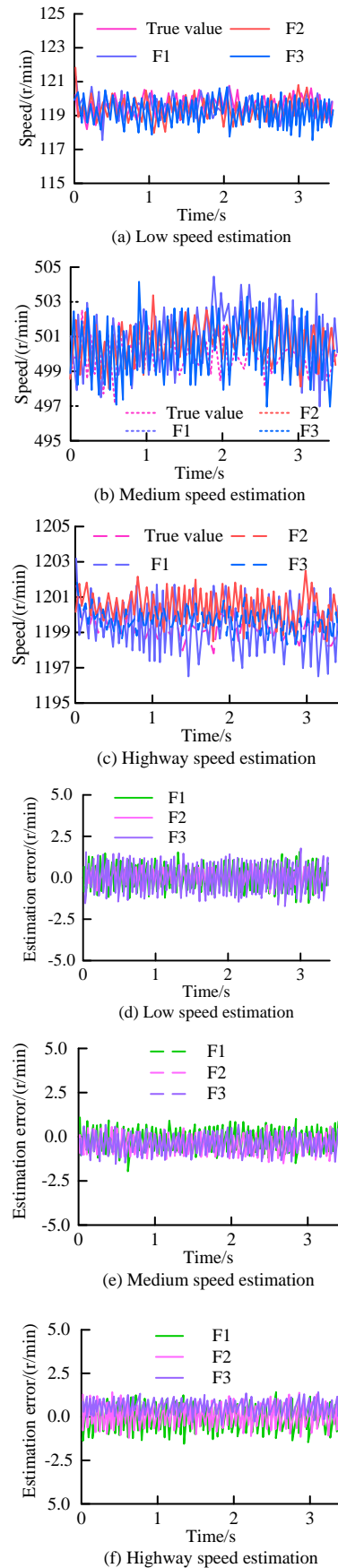


Fig. 7. Speed estimation and estimation error results based on different methods under different speed conditions

conditions, while F2 and F3 are selected under medium to high-speed conditions. To further compare the performance of different methods, this study conducts three experiments for each method under various speed conditions, as listed in Table 1.

Table 1. Comparison of MSE results based on different methods under different speed conditions

| Speed conditions | Number     | RMSE/(r/min) |        |        |
|------------------|------------|--------------|--------|--------|
|                  |            | F1           | F2     | F3     |
| Low speed        | 1          | 0.8006       | 0.9075 | 2.2492 |
|                  | 2          | 0.7978       | 0.9124 | 2.2473 |
|                  | 3          | 0.7923       | 0.9203 | 2.2614 |
|                  | Mean value | 0.7969       | 0.9134 | 2.2526 |
| Medium speed     | 1          | 1.1035       | 0.7786 | 0.5902 |
|                  | 2          | 1.0917       | 0.7812 | 0.5795 |
|                  | 3          | 0.9996       | 0.7865 | 0.5823 |
|                  | Mean value | 1.0649       | 0.7821 | 0.5840 |
| High speed       | 1          | 1.2613       | 0.8592 | 0.4998 |
|                  | 2          | 1.2495       | 0.8572 | 0.5175 |
|                  | 3          | 1.2501       | 0.8785 | 0.5002 |
|                  | Mean value | 1.2536       | 0.8650 | 0.5058 |

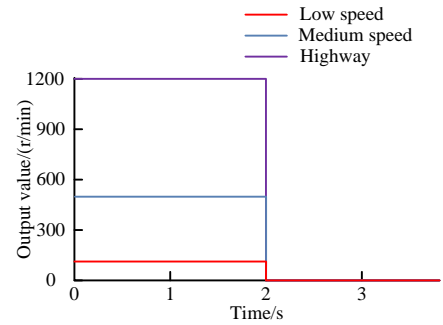
In Table 1, under low-speed conditions, the average RMSE of F1, F2, and F3 are 0.7969, 0.9134, and 2.2526, with F1 and F2 performing better. Under medium speed conditions, the average RMSE of each method is 1.0649, 0.7821, and 0.5840, with F2 and F3 performing better. Under high-speed conditions, F2 and F3 still perform better. In summary, it has been determined that F1 and F2 speed estimators will be used as feedback for speed information under low-speed conditions, while F2 and F3 will be used for medium and high-speed conditions.

**4.2. Simulation results of FD and FTC based on ESV algorithm**

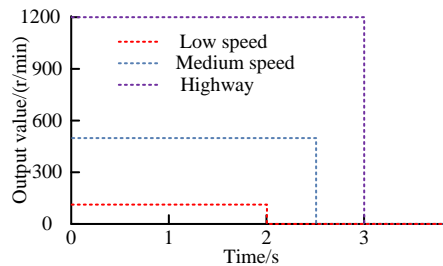
To verify the simulation performance of FD and FTC methods based on ESV algorithm, this study first diagnoses the wire breakage fault and FTC, and also uses the corresponding optimal speed estimator for feedback at different speed stages. Due to the fact that in the testing of FD and FTC, the main focus is on exploring the instantaneous performance of speed sensors after various faults occur. A simulation step size that is too large can cause significant errors, while a shorter step size may lead to excessive computational complexity. The aim is to ensure the stability and accuracy of simulation results. The simulation cycle is set to 3 seconds. From this, the diagnostic effectiveness of different fault occurrence research methods can be obtained, as shown in Fig. 8.

Figures 8 (a) and (b) show the output values of fault A and B at different speed stages, and Fig.8 (c) shows the feedback results of fault FD at different speed stages. In 8 (a) and 8 (b), when a disconnection fault occurs, the output values of the AM speed

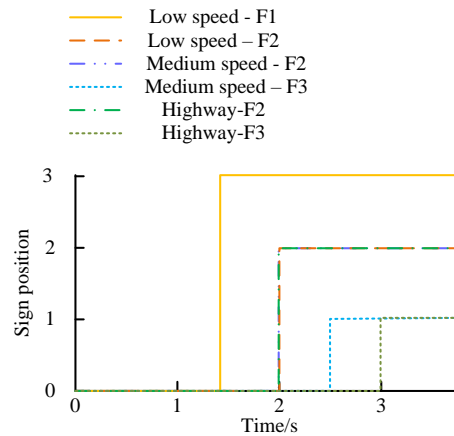
sensor will quickly become 0 at different speed stages. Under the low-speed condition in 8 (c), the output flag has 3 and 2, with the former selecting F1 speed estimator as feedback and the latter selecting F2. Under medium to high speed conditions, the output flag has 2 and 1, corresponding to F2 and F3 as feedback, respectively. To further analyze the feasibility of the research method under different speed conditions, the speed feedback curve corresponding to the insertion of a wire break fault is analyzed, as shown in Fig. 9.



(a) Output result of disconnection fault A



(b) Output result of disconnection fault B



(c) Feedback results

Fig. 8. The output values of wire breakage faults at different speed stages and the change curve of the marking line

Figures 9 (a) to (c) show a comparison of the speed feedback results of the optimal speed estimator under low-speed, medium speed, and high-speed conditions. In Fig.9, under various speed conditions, the fluctuation of the speed change curve is very small before the fault happens, while after the fault occurs, the speed change curve will experience significant fluctuations. The system can quickly switch to speed sensorless mode and determine the

optimal speed estimator for feedback through ESV algorithm. This confirms the effectiveness of the research method in FTC. To further evaluate the diagnostic effectiveness of the research method when a fixed deviation fault occurs, output values and feedback results are used for evaluation, as shown in Fig. 10.

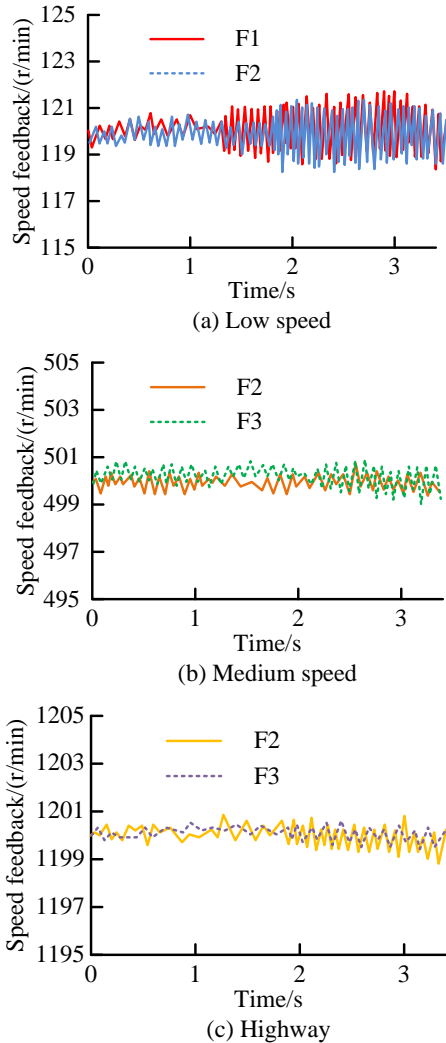


Fig. 9. Comparison of speed feedback results under different speed conditions

Figures 10 (a) and (b) show the output values of fixed deviation faults A and B at different speed stages, and 10 (c) is the feedback result at the time of occurrence. 10 (a) and 10 (b) show that after a fixed deviation fault occurs, the output value differs from the original normal value by a constant value of 10. In 10 (c), there are three types of output flags for feedback: 1, 2, and 3, corresponding to F3, F2, and F1. The above results can accurately provide speed feedback and performance when various faults occur. To further analyze the feasibility of using research methods for FTC, this study conducts experiments under different speed conditions, as shown in Fig. 11.

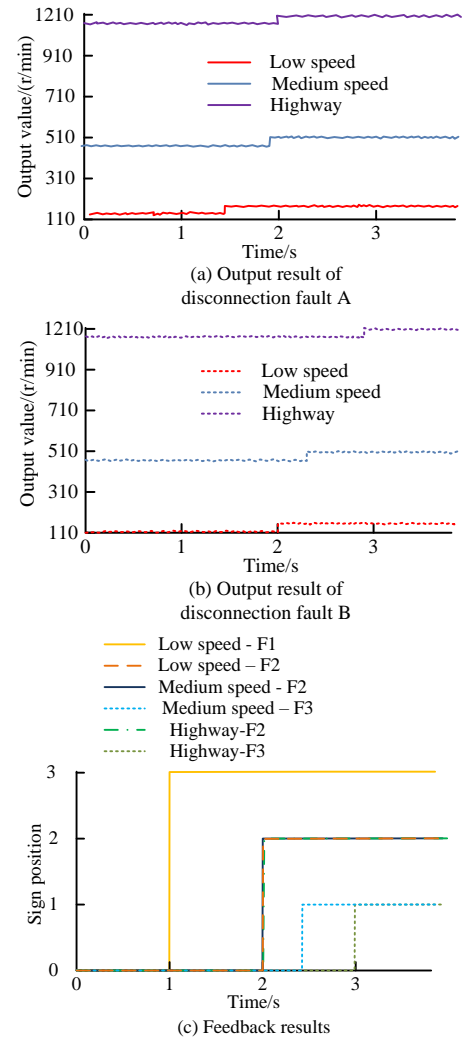
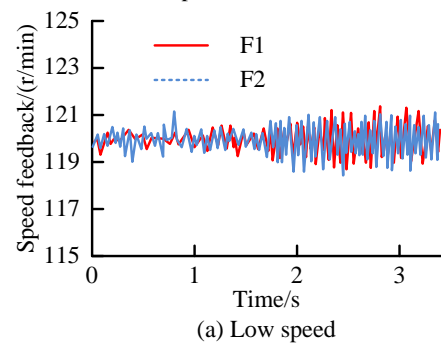


Fig. 10. Output results and feedback marker line results for fixed deviation faults under different speed conditions



Figures 11 (a) to 11 (c) show the feedback results of the AM speed sensor FD and FTC methods based on the ESV algorithm under low-speed, medium speed, and high-speed conditions. In Fig. 11, before the fault occurs, the speed feedback curve is relatively flat, while at the time of the fault, the speed feedback curve will experience significant fluctuations. After the occurrence of fixed deviation faults A and B, the AM closed-loop control system will quickly adjust to the sensorless model and use



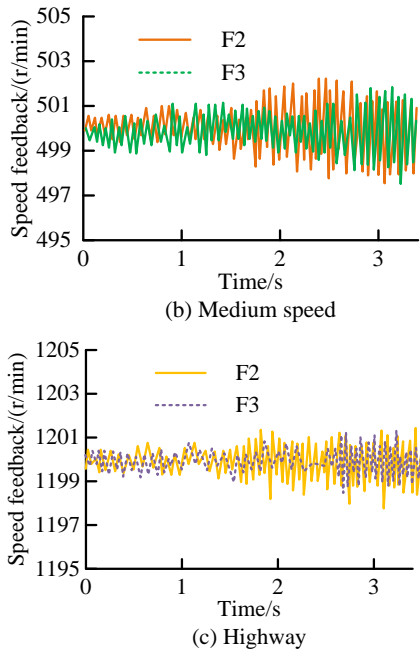


Fig. 11. Feedback findings from the fault diagnostic of the AM rate detector and the error-tolerant control technique based on the ESV algorithm at various speeds

the ESV algorithm to determine the optimal feedback method. This confirms the effectiveness and superiority of the research method in simulation. To further explore the robustness of the research method, two scenarios are set up. Scenario A: setting up a dynamic acceleration and deceleration process. Scenario B: Introducing dynamic load. The result change curve of scenario A can be obtained from this, as shown in Fig.12.

Figures 12 (a) to 12 (d) correspond to the results of speed, stator flux, torque, and A-phase stator current during the process from 300r/min to 700r/min, respectively. Figures 12 (e) to 12 (h) show the results of the dynamic changes in speed, stator flux, torque, and A-phase stator current from 700r/min to 300r/min. Fig.12 shows that the research method has excellent decoupling control effects on stator flux and instantaneous torque in dynamic processes. This indicates that the research method still exhibits good robustness in dealing with dynamic changes in situations. The control effect of the research method under scenario B is shown in Fig.13.

Figures 13 (a) and 13 (b) correspond to the active power and voltage variation curves of the research method under scenario B. The MSE of the voltage error controlled by the research method is only 0.6V, and the adjusted active power distribution is 1029kW. The results indicate that the research method has excellent tracking effect on the reference signal, and has a good response to dynamic load interference with strong randomness, significantly improving the stability and robustness of AMs. To present and analyze the above results more clearly, the study summarizes and processes the results, and the specific results are shown in Table 2.

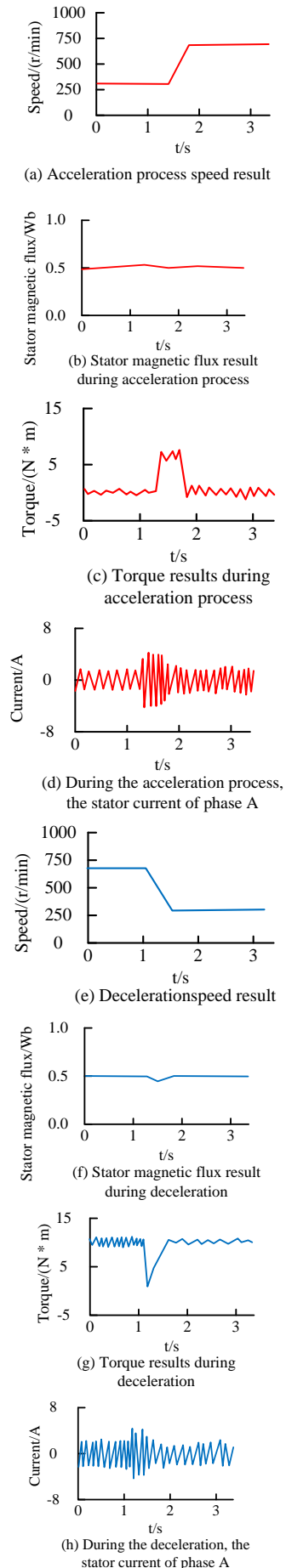


Fig. 12. The result change curve of scenario A

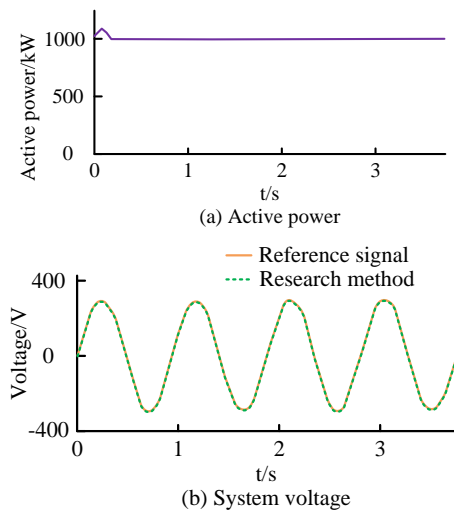


Fig. 13. The control effect of research methods under scenario B

Table 2. Summary table of research results

| Evaluation                   | Method | Low speed | Medium speed | High speed |
|------------------------------|--------|-----------|--------------|------------|
| MSE                          | F1     | 0.7969    | 1.0649       | 1.2536     |
|                              | F2     | 0.9134    | 0.7821       | 0.8650     |
|                              | F3     | 2.2526    | 0.5840       | 0.5058     |
| Disconnected fault output    | F1     | 0         | 0            | 0          |
|                              | F2     | 0         | 0            | 0          |
|                              | F3     | 0         | 0            | 0          |
| Fixed deviation output value | F1     | 130       | 510          | 1210       |
|                              | F2     | 130       | 510          | 1210       |
|                              | F3     | 130       | 510          | 1210       |

According to Table 2, the proposed method of combining different speed estimators can control errors within the fault-tolerant range across the entire speed range in the results of wire breakage faults and fixed deviation faults. This approach ensures the stable operation of the control system. In addition, in the MSE results, different speed estimators have their own advantages in each speed range, and the research method can fully utilize the control performance of different speed estimators in the full speed stage. In summary, although multiple experiments are conducted to obtain a reasonable threshold in the presence of external interference during the operation of the control system, the research method achieves good control results overall and obtains a more reliable and fault-tolerant approach.

## 5. CONCLUSION

The continuous development of power electronics technology and modern control theory provides new possibilities for the application of AM in various fields. However, its vector control system requires efficient acquisition of current and rotor related information, and the performance and cost of

speed sensors are greatly limited. To address the above issues, the study first constructed an AM mathematical model and corresponding control method, then proposed a novel speed estimation method that combines three speed estimators. Finally, the study designed an AM speed sensor FD and FTC method based on the ESV algorithm. Experiments have shown that under low-speed conditions, the average RMSE of F1, F2, and F3 were 0.7969, 0.9134, and 2.2526, and the speed estimators corresponding to F1 and F2 had a higher degree of fit with the actual values. Under medium and high speed conditions, the speed estimators corresponding to F2 and F3 performed better. When faults occurred at random time points in different speed stages, the speed variation curve would experience significant fluctuations. The research method could quickly determine the optimal speed estimator and quickly switch to sensorless mode, controlling the speed error within a range of  $\pm 5\pi/\text{min}$ . Within this range, the speed sensor of AM could still ensure safe and stable operation. In summary, the simulation results have verified the effectiveness and feasibility of the method of combining multiple speed estimators for FD and FTC, ensuring that the AM speed sensor can still operate safely and smoothly after a fault occurs. However, there are still shortcomings in the research. The research method only simulates the results under constant speed conditions. Therefore, in future research, variable speed conditions can be set for simulation to expand the application scope and effectiveness of the research method.

**Source of funding:** *This research received no external funding.*

**Declaration of competing interest:** *The author declares no conflict of interest.*

## REFERENCES

- Fadi A, Ahmad A, Rabia S, Cristina M, Ibrahim K. Velocity sensor fault-tolerant controller for induction machine using intelligent voting algorithm. *Energies*. 2022;15(9):3084. <https://doi.org/10.3390/en15093084>.
- Negadi K, Mansouri A, Marignetti F, Touan M. An MRAS based estimation method with artificial neural networks for high performance induction motor drives and its experimentation. *International Review of Automatic Control (IREACO)* 2014; 7(2):123-130.
- Saha S, Kar U. Signal-based position sensor fault diagnosis applied to pmsm drives for fault-tolerant operation in electric vehicles. *World Electric Vehicle Journal*. 2023;14(5):123. <https://doi.org/10.3390/wevj14050123>.
- Bensikaddour EH, Boutte A. Motor speed control using a fault tolerance implementation on SRAM-based FPGA. *Algerian Journal of Engineering and Technology*. 2023;8(2):302-308. <https://doi.org/10.57056/ajet.v8i2.137>.
- Negadi K, Mansouri A, Khtemi B. Real time implementation of adaptive sliding mode observer based speed sensorless vector control of induction

- motor. *Serbian Journal of Electrical Engineering*. 2010. (7)2:167-184. <https://doi.org/10.2298/SJEE1002167N>.
6. Zhang D, Han H, Yang YHY. Modeling and anti-swing control of quadrotor-suspended system with variable cable length at unequal speed. *Transactions of the Institute of Measurement and Control*. 2024; 46(6): 1177-1189. <https://doi.org/10.1177/01423312231187446>.
  7. Shao N, Liu L, Fang LY. Adaptive sliding mode observers-based dissipative Hamilton finite time optimization control for the speed and tension system of reversible cold strip rolling mill. *International Journal of Adaptive Control and Signal Processing*. 2024;38(3):907-920. <https://doi.org/10.1002/acs.3731>.
  8. Layate Z, Tahar B, Salima L. Dynamic flow control of a photovoltaic pumping system-based asynchronous induction motor. *International Journal of Nonlinear Dynamics and Control*. 2019;1(3):255-270. <https://doi.org/10.1504/IJNDC.2019.10020141>.
  9. Tegui JB, Kammogne AST, Gammene SGT, Siewe MS, Kenne G. Fuzzy-enhanced robust fault-tolerant control of IFOC motor with matched and mismatched disturbances. *Mathematical Foundations of Computing*. 2022;5(4):295-314. <https://doi.org/10.3934/mfc.2022006>.
  10. Daoudi SE, Lazrak L, Ouanjli NE, Lafkih MA. Applying sliding mode technique for the nonlinear DTC-SPWM control strategy of sensorless squirrel cage asynchronous motor. *International Journal of Dynamics and Control*. 2021;9(4):1633-1644. <https://doi.org/10.1007/s40435-021-00758-8>.
  11. Li Y, Li F, Lu C, Fei J, Chang B. Composite fault diagnosis of traction motor of high-speed train based on support vector machine and sensor. *Soft Computing: A Fusion of Foundations, Methodologies and Applications*. 2023;27(12):8425-8435. <https://doi.org/10.21203/rs.3.rs-2549787/v1>.
  12. Xia Y, Xu Y, Gou B. Current sensor fault diagnosis and fault-tolerant control for single-phase PWM rectifier based on a hybrid model-based and data-driven method. *IET Power Electronics*. 2021;13(18): 4150-4157. <https://doi.org/10.1049/iet-pel.2020.0519>.
  13. Gholipour A, Ghanbari M, Alibeiki E, Jannati M. Speed sensorless fault-tolerant control of induction motor drives against current sensor fault. *Electrical Engineering*. 2021;103(3):1493-1513. <https://doi.org/10.1007/s00202-020-01179-0>.
  14. Shabbir W, Aijun L, Yuwei C. Neural network-based sensor fault estimation and active fault-tolerant control for uncertain nonlinear systems. *Journal of the Franklin Institute*. 2023;360(4):2678-2701. <https://doi.org/10.1016/j.jfranklin.2022.12.044>.
  15. Niazi IK, Navid MS, Rashid U, Amjad I, Olsen S, Haavik H, Alder G, Kumari N, Signal N, Taylor D. Associative cued asynchronous BCI induces cortical plasticity in stroke patients. *Annals of Clinical and Translational Neurology*. 2022;9(5):722-733. <https://doi.org/10.1002/acn3.51551>.
  16. Qin Y, Sun Z. Memory dynamic output feedback controller based on asynchronous event-triggered robust H-infinity control for nonlinear ICPSs under data injection attacks. *International Journal of Robust and Nonlinear Control*. 2022;32(3):1904-1921. <https://doi.org/10.1002/rnc.5919>.
  17. Guo Z, Tong D, Zhao YC, Chen S, Nai JQ, Ye MH. Efficiency optimization of variable iron loss resistance asynchronous motor based on grey wolf optimization algorithm. *Journal of Electrical Engineering & Technology*. 2024;19(1):485-493. <https://doi.org/10.1007/s42835-023-01561-5>.
  18. Bandewad G, Datta KP, Gawali BW, Pawar, SN. Review on discrimination of hazardous gases by smart sensing technology. *Artificial Intelligence and Applications*. 2023;1(2):86-97. <https://doi.org/10.47852/bonviewAIA3202434>.
  19. Saminu S, Xu G, Zhang S, Kader IAE, Aliyu HA, Jabire AH, Ahmed YK, Adamu MJ. Applications of artificial intelligence in automatic detection of epileptic seizures using EEG signals: A review. *Artificial Intelligence and Applications*. 2023; 1(1): 11-25. <https://doi.org/10.47852/bonviewAIA2202297>.
  20. Ebrahim OS, Badr MA, Elgendy, Ali S, Jain PK, Shawky KO. Neural network based robust optimal energy control of pulse width modulation-inverter fed motor driving pump. *IET Electric Power Applications*. 2023;17(10):1334-1346. <https://doi.org/10.1049/elp2.12345>.



**Qiubo LI** graduated from Jiangsu University with a bachelor's degree in automation in 2003, has been working in Jiangsu Maritime Vocational and Technical College since 2003, engaged in the teaching of basic courses of automation technology.  
e-mail: [13914750290@163.com](mailto:13914750290@163.com)